Halogen Effects on Ordering and Bonding of $CH_3NH_3^+$ in $CH_3NH_3PbX_3$ (X = Cl, Br, I) Hybrid Perovskites: A vibrational spectroscopic study

Ralf G. Niemann,[a ‡] Athanassios G. Kontos, [b‡] Dimitrios Palles,[c] Efstratios I. Kamitsos,[c] Andreas Kaltzoglou,[b] Federico Brivio,[a] Polycarpos Falaras,[b] and Petra J. Cameron[a]*

[a] Department of Chemistry, University of Bath, Bath BA2 7AY, United Kingdom

[b] Institute of Nanoscience and Nanotechnology, NCSR Demokritos, 15310 Athens, Greece

[c] Theoretical and Physical Chemistry Institute, National Hellenic Research Foundation, 11635 Athens, Greece

ABSTRACT: This study reports Raman and infrared spectra of hybrid organic-inorganic $MAPbX_3$ perovskites (MA = CH_3NH_3, X = Cl, Br, I) and their mixed-halide derivatives. Raman spectra were recorded at three laser wavelengths (514, 785 and 1064 nm) under on- and off-resonance conditions, as well as at room temperature and 100 K. Use of different excitation wavelengths allowed the unambiguous acquisition of 'true' Raman spectra from the perovskites, without degradation or photo-induced structural changes. Low frequency PbX vibrational modes were thoroughly identified by comparison of Raman and far-IR results. Red Raman frequency shifts for almost all MA vibrations from 200-3200 cm^{-1}, particularly intense for the torsional mode, were observed towards heavy halide derivatives, indicative of strengthening the interaction between halides and the organic cation inside the inorganic cage. Different MA-X bonding schemes are evidenced by torsional mode pairs emerging at the orthorhombic phase. $MAPbBr_3$ was further characterized by variable temperature Raman measurements (100-295 K). Broadening of the MA rocking mode slightly above the tetragonal I to II phase transition is connected with disorder of the MA cation. Our results help understanding perovksite materials properties (ferroelectric domain formation, anomalous hysteresis) and their use as efficient light absorbers in solar cells.

1. INTRODUCTION

Recently, there has been an increase of research into perovskite materials [1-6] leading to a steep rise in cell performances to a certified value of 21 %[7] within a few years. Similar developments took decades for other photovoltaic technologies to achieve. Even though perovskites are a large family of compounds which all share the common stoichiometry ABX_3, most of the recent attention has been given to the hybrid organic-inorganic methyl ammonium lead halide perovskites ($MAPbX_3$, MA = methyl ammonium, Pb = lead, X = halide) and in particular the iodide derivative $MAPbI_3$. Structure and bandgap in ABX_3 perovskites can be easily modified by changing the cation, the metal or the halide. Partial substitution of the iodide in $MAPbI_3$ results in the iso-structural $MAPbI_{3-x}Br_x$ with a blue-shifted bandgap, which is favorable for multi-junction devices and increases chemical stability[8-11]. However, the photo-instability of the excited state of $MAPbI_{3-x}Br_x$ results in segregation of the material into micro-domains for $x > 0.6$[12]. Addition of chloride during perovskite crystallization has been shown to improve charge transport[13,14] even though its exact role remains unclear[15,16]. Besides the influences of chemical composition on optoelectronic performance and stability, temperature-dependent structural changes play a pivotal role as well. The low-temperature orthorhombic phase of $MAPbI_3$ is intrinsically more stable compared to the tetragonal phase obtained at room temperature[10] and charge-carrier dynamics become more confined and show excitonic behavior in the orthorhombic phase[17]. This indicates that temperature-induced structural changes can tip the scales from an exothermic towards endothermic dissociation enthalpy and from free charge-carrier movement to excitonic confinement. Thus tuning of the perovskite composition or structure can be used in order to enhance stability and performance of perovskite solar cells, both of which are investigated in this study.

X-ray diffraction has been widely used to determine the crystal structure of $MAPbX_3$ perovskite materials after their discovery in 1978[18,19] . However, it can be difficult to resolve the positions of lighter atoms like nitrogen and carbon in the presence of the heavier lead and iodine. The structural orientation of the MA cation within the inorganic framework has therefore been studied in more detail with NMR spectroscopy[20] and neutron scattering[21,22]. These studies were able to resolve the orientation of MA cations and show an increasing disorder when moving from the orthorhombic phase towards higher temperature phases alongside a weakening of the bonding between the NH_3 in the MA and the halides[21,22]. Alignment of the MA cations can yield a net dipole that is energetically favorable in the tetragonal phase and is further stabilized in the orthorhombic perovskite phase. It has been suggested that this MA alignment can induce polar-ferroelectric characteristics in the material in low symmetry phases[23]. Structural dynamics within the perovskite structure have important implications on the operation mechanism of perovskite solar cells. They are thought to assist charge separation[24], tune the band gap[25,26] , improve open-circuit voltage[27] and affect hysteresis during current-voltage measurements[28]. These versatile implications show the importance of a detailed study of MA dynamics with Raman and IR spectroscopies.

Perovskite halides have been examined before with mid-IR absorption experiments[29-32] which give valuable information about MA dynamics, hydrogen bonding and water infiltration inside the perovskites, but do not cover the important low-frequency range where vibrations of the inorganic lead halide network of corner sharing PbX_6 octahedra are mainly active. Despite the suitability of the infrared absorption technique for obtaining the vibrational modes in light sensitive systems, only limited far-IR data for single halide perovskite compounds have been reported up to now[33,34]. Besides, reports of Raman measurements on $MAPbI_3$ perovskites [23,35-40]

have so far been limited to resonant or near resonant conditions with typical excitation wavelengths of 514 nm, 532 nm or 785 nm. However, this may be problematic because of the high absorbance and photo-sensitivity of the material. Moreover, the Raman spectrum of $MAPbI_3$ at low frequencies resembles the PbI_2 precursor spectrum, which makes it difficult to distinguish between pristine and (partially) decomposed samples, as we pointed out recently[41]. Ledinsky et al. reported on photo-induced decomposition during resonant Raman measurements and emphasized the use of laser intensities far below the values that would usually be employed[36]. Apart from the photo-induced decomposition[42], $MAPbI_3$ photo-excitation induces a range of other effects that can alter its structure and therefore the experimental outcome[12,37,43]. As mentioned earlier, mixed-halide perovskites have been shown to segregate into micro-domains under illumination, presumably caused by an instability of the photo-excited state[12]. A recent study by Gottesman et al. showed reversible structural modifications of $MAPbI_3$ in the Raman spectrum by excitation under resonant conditions[39]. Experimental results are often backed by computational studies[23,37,38], which give valuable information. Nevertheless, these calculations are based on several assumptions and produce complex spectra with many superimposed lines especially in the low-frequency range. Also, small uncertainties involved in calculations can result in very large offsets in the resulting spectrum, making peak assignment ambiguous[37].

The current work investigates $MAPbX_3$ structural dynamics for all halide derivatives by combining far-IR absorption and Raman scattering and addresses most of the critical issues raised by the literature up to now. For the first time we perform off-resonance Raman experiments and manage to obtain unambiguous Raman spectra avoiding decomposition or structural changes in the material. Measurements have also been carried out on the low-

frequency Raman and IR active modes of the inorganic PbX_6 octahedra. Variable temperature comparative Raman measurements show characteristic spectroscopic changes of the MA torsion and rocking vibrations which have implications on the ordering and bonding of MA inside the inorganic framework. Understanding the fundamental material properties is the key to the construction of perovskite solar cells with improved efficiency and stability.

2. EXPERIMENTAL METHODS

2.1 MATERIALS AND DEPOSTION OF FILMS

The methylammonium halide salts (MAI, MABr and MACl) were synthesized by drop-wise neutralization of an ice-bath cooled solution of 24 mL methylamine (Sigma-Aldrich) in 100 mL of ethanol with the corresponding hydrogen-halide (10 mL of 57 wt% HI in water; 14.6 mL of 48 wt% HBr in water; 15 mL of 37 wt% HCl in water; all Sigma-Aldrich). The solvent was removed in a rotary evaporator and the powder was recrystallized from ethanol. Upon slow cooling of the ethanol solution white crystals were formed. Washing with diethylether and drying at 70 °C for 6 h was performed afterwards. The single halide perovskite ($MAPbI_3$, $MAPbBr_3$ and $MAPbCl_3$) precursor solutions were prepared by mixing a 1:1 stoichiometric ratio of lead(II) halide (PbI_2, 99 %; $PbBr_2$, 99.99 %; $PbCl_2$, 99.99 %; all Sigma-Aldrich) with the corresponding methylammonium halide at a 1 mol/L concentration in DMSO (≥ 99.9 %; Sigma-Aldrich) for 1 h at 60 °C. For the mixed halide perovskite precursor solutions, the respective ratios of single halide solutions were mixed and stirred for 1 h. Synthesis of the precursor salts was performed in the fume hood, while the mixing of the perovskite precursor solutions, films deposition as well as annealing were done in an Argon-filled glovebox (H_2O and O_2 concentration < 1 ppm).

For planar films the precursor solution was deposited on a microscope glass slide. For mesoporous films, a dispersion of Al_2O_3 nanoparticles (20 wt% in 2-propanol; Sigma-Aldrich) was spin-coated onto glass slides (2000 rpm for 60 s) and annealed at 500 °C for 30 min. All perovskite solutions were spin-coated onto the flat or mesostructured substrates at 2000 rpm for 60 s and then annealed on a hotplate at 100 °C for 30 min. Samples for far-IR characterization were prepared by depositing mesoporous perovskite films on a 0.8 mm thick high density polyethylene (HDPE) to improve surface wettability. In order to enhance the perovskite Raman scattering volume, measurements were performed on powder samples taken by scratching the films.

2.2 CHARACTERIZATION

The perovskite films were structurally characterized using a Siemens D-500 diffractometer, that operates in Bragg-Brentano geometry with Cu $K_{\alpha 1}$ radiation (λ = 1.5406 Å) and Cu $K_{\alpha 2}$ radiation (λ = 1.5444 Å). Data were collected over the angular range 5 ° ≤ 2θ ≤ 100 ° counting for 1 s at each step of 0.05 ° in detector position. Unit-cell refinements were performed with GSAS package[44].

UV-Vis Diffuse Reflectance (R) spectra were acquired on a Hitachi 3010 spectrophotometer using an integrating sphere with 60 mm diameter and $BaSO_4$ as a reference. The data were transformed into Kubelka-Munk absorbance $F(R)= (1-R)^2/2R$.

The IR transmittance measurements were run at normal incidence on a Bruker Vertex 80v vacuum spectrometer using HDPE-Alumina films as a reference. Each spectrum was averaged over 200 scans with a 4 cm^{-1} resolution. The far-infrared (FIR) beamsplitter and detector used

offered a working range of ca. 60 cm^{-1} to 680 cm^{-1}. The transmittance spectra were converted to absorbance and normalized to 1.

Raman measurements with excitation at 514 nm and 785 nm were performed with a Renishaw In-Via Reflex dispersive micro-Raman spectrometer with <2 cm^{-1} resolution. The laser beam was focused on a spot of 1 μm in diameter with a x100 magnification lens. Rayleigh scattering was rejected with 50 cm^{-1} or 110 cm^{-1} cut-off dielectric edge filters, and analysis of the scattered beam was performed on a 250 mm focal length spectrometer along with suitable diffraction gratings (1800 lines/mm for visible and 1200 lines/mm for NIR) and a high-sensitivity CCD detector. Cryostatic Raman measurements at low temperature (LT) were done under inert atmosphere in a THMS600PS Linkam cell by focusing the laser beam with a x50 long focal distance lens. Raman spectra under off-resonance conditions for all samples were acquired with a Bruker RFS100 FT-Raman spectrometer equipped with a Nd-YAG laser emitting at 1064 nm. Each spectrum was averaged over 100 scans or 200 scans with 4 cm^{-1} resolution, while the effective working range was ca. 100 cm^{-1} to 3500 cm^{-1}. All RT Raman measurements were performed in air and at different laser powers to assure that the intensities used did not induce changes in the spectra. The measured Raman spectra present a strong elastic scattering background in the low-frequency (LF) spectral range. In order to enhance the Raman features at this LF range where very informative PbX and MA vibrations are active, and correctly determine spectral characteristics (frequency, linewidth and line shape), the spectra were temperature-reduced using the expression of eq. (1)[45]:

$$I_{red}(\omega) = I(\omega)\frac{1}{\mathrm{n}(\omega,T)+1},\ \mathrm{n}(\omega,T) = \left(exp^{\frac{hc\omega}{k_BT}} - 1\right)^{-1} = \left(exp^{\frac{1.44\,\omega}{T}} - 1\right)^{-1}, \qquad (1)$$

where $I(\omega)$ and $I_{red}(\omega)$ are the measured and reduced Raman intensity, respectively. $n(\omega,T)$ is the Bose-Einstein statistic factor, h and k_B are the Planck and Boltzmann constants, respectively, c is the speed of light, ω is the Raman shift in cm^{-1} and T is the temperature in K. The analysis of the reduced spectra was done by fitting them with mixed Lorenzian-Gaussian functions using the Wire software from Renishaw. Linewidths were corrected for instrumental broadening.

3. RESULTS AND DISCUSSION

3.1 STRUCTURAL AND OPTICAL CHARACTERIZATION

Schemes of the perovskites structure at the three different structural modifications (cubic, tetragonal and orthorhombic) together with transition temperatures[46] are shown in Figure 1a. Powder-XRD patterns of the area of interest for the whole set of $MAPbX_{3-x}Y_x$ materials, shown in Figure 1b, confirm the presence of the perovskites as the main phase. In addition, certain amounts of admixtures were present, in particular PbI_2 for the I-containing samples (for the full patterns see Figure S1 in the Supporting Information). $MAPbCl_3$, $MAPbBrCl_2$, $MAPbBr_2Cl$ and $MAPbBr_3$ were indexed as cubic systems, whereas $MAPbBr_2I$, $MAPbBrI_2$ and $MAPbI_3$ were indexed as tetragonal systems, in accordance to ref. [8]. A regular trend in the unit-cell expansion with substitution of Cl by Br and I was observed. The determined lattice parameters of the tetragonal $MAPbI_3$ (a = b = 8.861(2) Å, c = 12.653(4) Å) are in agreement with the literature values of a = b = 8.849(2) Å, c = 12.642(2) Å[47], within the 3σ estimated standard deviation. The lattice parameters are given in Table S1 of Supporting Information.

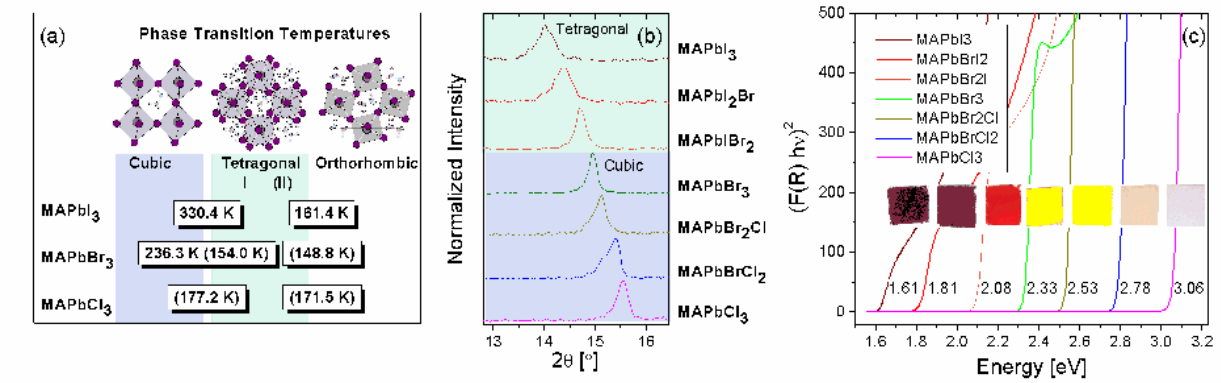

Figure 1: (a) The different phases of the $MAPbX_3$ perovskite, which transform upon changing temperature or halide composition; halides: large purple spheres, Pb: large grey spheres and MA: interstitial. Transition temperatures into tetragonal II $MAPbBr_3$ are in brackets. **(b)** Powder XRD patterns of the range of interest from all halide perovskites examined in this study. **(c)** UV-Vis spectra (where F(R) is the Kubelka-Munk function) of perovskite films which change in color (from dark brown to white) and show a shift in band gap energy (from 1.61 to 3.06 eV) as lighter halides are introduced into the structure.

Substitution of heavy halogen atoms with lighter ones in $MAPbX_{3-x}Y_x$ results in films with tunable color from dark brown to white, as shown by the photographs of the prepared films inserted in Figure 1c. In order to analyze the light harvesting of the films over the solar spectrum diffuse reflectance measurements were carried out. In Figure 1c, the absorption F(R) data are plotted in terms of $(F(R)h\nu)^2$ vs. hν, which is the standard analysis for materials having a direct band gap. Band gap values (E_g) were found by the intersections of the slope with the energy-axis and are shown upon the graphs, and further listed in Table S2 where they are compared with the Raman excitation energies. The values are slightly blue-shifted compared to literature values[8]. Blue-shifted absorption onsets were reported recently[48,49]. The shift can be caused by a ferroelectric domain wall induced band gap reduction and has been observed for mesoporous

scaffold architectures[26,48]. The influence of annealing temperature on band gap is another possible explanation for this observation[49]. In general, the reported band gaps for MA lead perovskites can vary significantly[50]. The excitonic peaks appearing in the spectra for lighter halide derivatives are presumably caused by an increase in the exciton binding energies[51].

3.2 LOW FREQUENCY Pb-X VIBRATIONAL MODES: FAR-IR AND MICRO-RAMAN RESULTS AT ROOM TEMPERATURE

The PbX_6 octahedra of the perovskite halides belong to the O_h point group symmetry and have two IR active modes, ν_3 and ν_4, with T_{1u} symmetry and three Raman active modes ν_1, ν_2 and ν_5, with A_{1g}, E_g and T_{2g} symmetry, respectively[37,52]. Splitting of the doubly and triply degenerate modes is expected due to distortion of the octahedra, a) by interaction between the methylammonium and certain halogen atoms, and b) by the occupation of the octahedral corners with different halide atoms in the complex halide derivatives. According to theoretical calculations[37], the splitting is considerably larger for the Cl based perovskites (Cl has the strongest electronegativity). In the present study, and for the first time in the literature, both the IR and Raman low-frequency Pb-X vibrational modes have been observed for all members of the $MAPbX_3$ family.

Far-IR spectra obtained for all $MAPbX_3$ derivatives are shown in the range of 50-300 cm^{-1} in Figure 2a. Broad spectralines are observed in all cases, justified by the polycrystalline character of the materials. Analysis of spectral components as well as spectrum of the HDPE-Alumina reference are shown in Figure S2. The spectra for $MAPbI_3$ present strong IR-activity below 120 cm^{-1}, which is mainly due to internal PbI_3 vibrations as shown in recent density functional perturbation theory calculations[34]. The spectra of the $MAPbBr_xI_{3-x}Br_x$ series are analyzed with

two component bands, which are straightforwardly attributed to the ν_3 asymmetric stretching (103-125 cm^{-1}) and ν_4 asymmetric bending (66-76 cm^{-1}) vibrations of PbX_6 octahedra. For the Cl containing samples, the higher frequency band is split into two component-bands, which are well described by mixed Lorenzian-Gaussian character. For the pure Cl perovskite, a very broad band is observed which includes both the ν_4 band, as a low frequency shoulder, as well as the split ν_3 band at higher frequencies. The peak positions of the deconvoluted ν_3 and ν_4 modes (two peaks for the Cl containing perovskites) are marked upon Figure 2a. In Figure 2b we plot the frequency of the two modes versus the halogen order. For the estimation of the ν_3 frequency for the mixed halides, a weight average of the two ν_3 related component bands was taken into account. First of all we should note that the ratio ν_4/ν_3 remains stable in the 0.60-0.64 range. The only exception is the pure Cl perovskite for which it is slightly larger and equal to 0.67, presumably due to uncertainties in the fitting of the corresponding broad far-IR band. The fixed ν_4/ν_3 ratio verifies self-consistency of the analysis, and the ratio values match the corresponding ratios for several other compounds quite well (e.g., the ratio for the $[PbCl_6]^{2-}$ anion from ref. [**Error! Bookmark not defined.**] is 0.54).

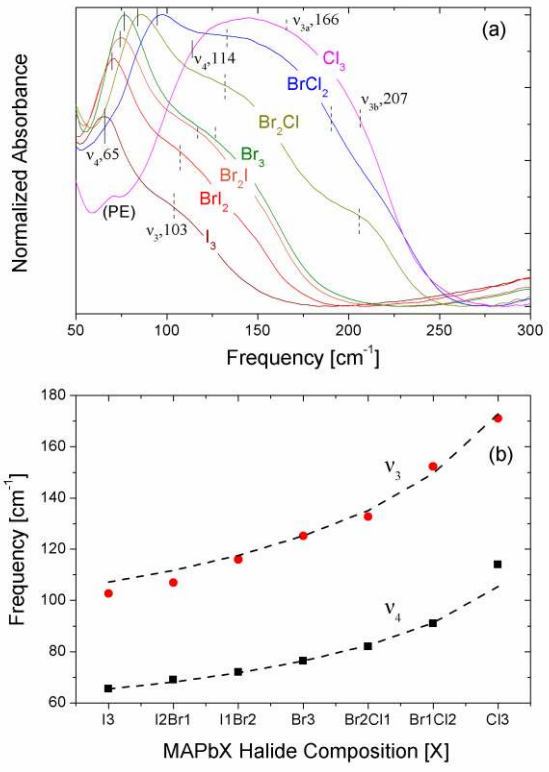

Figure 2 (a) Far-IR spectra for the various perovskite derivatives measured at RT. The band marked by PE is due to the polyethylene substrate. Peak frequencies of the ν_3 and ν_4 bands obtained by fitting the spectra (see Figure S2) are marked with dashed and solid lines, respectively. The values are noted for the end perovskite members, $MAPbI_3$ and $MAPbCl_3$. For Cl based perovskites the ν_3 band is split into two component bands, ν_{3a} and ν_{3b}. **(b)** Frequency of ν_3 (average) and ν_4 modes vs. halide composition. Dashed lines show predictions based on the harmonic oscillator model.

Both ν_3 and ν_4 modes shift to higher frequencies upon introduction of lighter halides in the structure. The ν_3 and ν_4 frequencies depend strongly on the reduced mass μ of the Pb-X bond and follow the model for a harmonic oscillator $\nu = (\frac{1}{2\pi})\sqrt{k/\mu}$, with the crude assumption of the same bond strength k for all halides. The reduced mass is $\mu^{-1} = m_{Pb}^{-1} + m_X^{-1}$ where m_X for the

composite perovskite halides was calculated by the weight average of the halogen atomic masses in their chemical formula. The model calculations have been done by weighting the ν_3 and ν_4 frequencies against those observed for $MAPbBr_3$ and are shown with dashed lines in Figure 2b. These results verify that the low-frequency IR active vibrations are of the inorganic Pb-X type and lack noticeable influence from the MA cation. A similar behavior which consolidates our argument is observed by analyzing the frequency shifts of the Sn-X modes in the analogous $[SnX_6]^{2-}$ octahedral system, irrespective of the vibration mode[52].

Complementary to the far-IR spectra, low frequency Raman spectra were obtained above 50 cm^{-1} with 785 nm laser line excitation. The spectra are presented in Figure 3a for all the perovskite compounds apart from the pure $MAPbI_3$ which showed only a strong photoluminescence (PL) response. The vibrational modes of the PbX_6 octahedra were observed below 250 cm^{-1}. At 270 cm^{-1} for $MAPbBrI_2$ and at higher frequencies for the rest of the compounds, a broad and well-formed band was observed. This band is due to the torsion of MA units and will be discussed in detail in the next section.

The Raman spectra below 230 cm^{-1} involve vibrations of Pb-X bonds consisting of heteropolar ionic/covalent interactions in the inorganic framework and show very broad multi-bands which are not easily resolved into components. The general trend is that all these measured bands increase in frequency by moving towards light halides following the corresponding behavior shown in the far-IR spectra. The multi-band character of the Raman features is clearer for the mixed perovskite derivatives and is justified considering the lifting in degeneracy of modes. As already discussed, three Raman bands due to the Pb-X vibrations of the octahedral structure are expected in the LF range. Among them the symmetric stretching mode ν_1 is expected to be the highest in frequency, followed with the asymmetric stretching mode ν_2 and the asymmetric

deformation v_5[52]. Since it is difficult to fit the spectra, we attempt an analysis based on the ratios of the frequencies between the various inorganic vibrational modes from the literature. Thus according to data in Ref [**Error! Bookmark not defined.**], the ratios $v_1/v_3 = 1.07$, $v_2/v_1 = 0.74$ and $v_5/v_1 = 0.49$ are observed for $[PbCl_6]^{2-}$ while similar values are found for other systems, too, such as for $[SnX_6]^{2-}$ and $[SbX_6]^{2-}$. Thus, based on our v_3 values from our far-IR analysis we have predicted the mean frequencies of the corresponding Raman bands. The respective calculated values of the three Raman modes are reported in Figure 3a and qualitatively describe the shifts observed as a function of the halide change. By extending the calculations for $MAPbI_3$, the mean frequencies for the three Raman active modes are predicted to be $v_1 = 110$ cm^{-1}, $v_2 = 81$ cm^{-1} and $v_5 = 54$ cm^{-1} (see also Figure 3a).

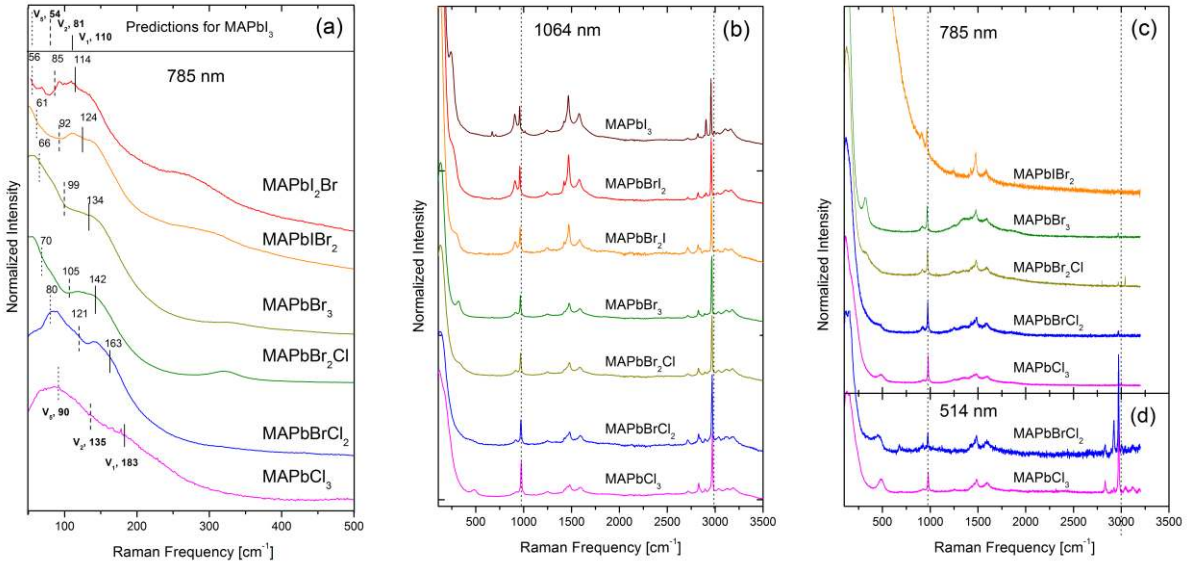

Figure 3: **(a)** Low frequency Raman spectra obtained by excitation at 785 nm. Peak frequencies of v_1 (solid line marks), v_2 (dashed line marks) and v_5 (dotted line marks) noted upon the graph are estimated from the experimentally recorded frequency of the v_3 IR band and modes

frequency ratios from the literature (for details see text). Raman spectra of the perovskite halide derivatives obtained by excitation at **(b)** 1064 nm, **(c)** 785 nm and **(d)** 514 nm, at RT.

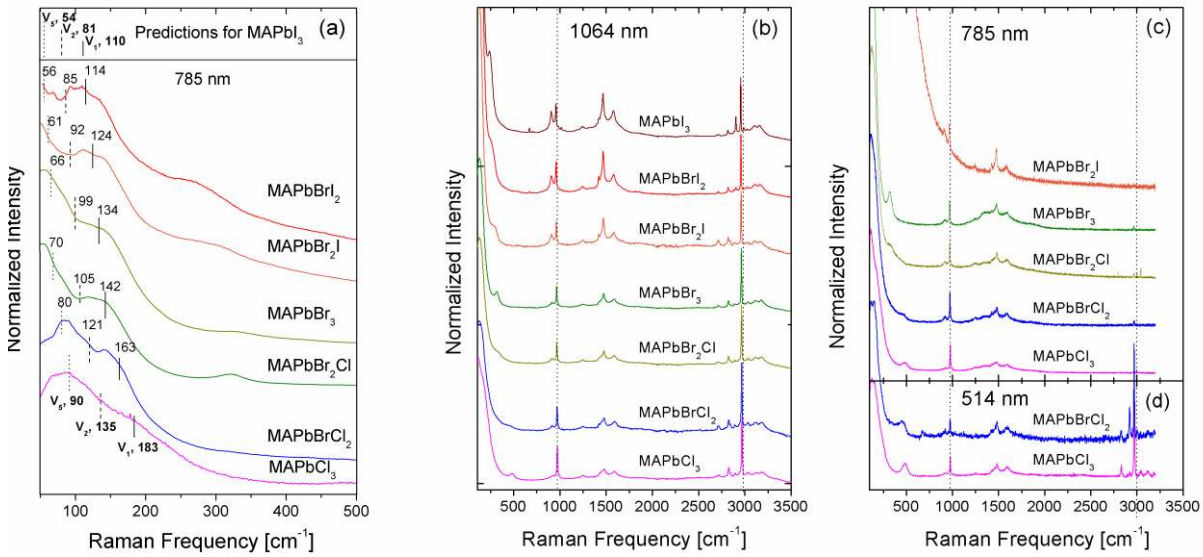

3.3 VARIABLE EXCITATION MICRO-RAMAN SPECTRA OF ALL PEROVSKITE DERIVATIVES

Extensive Raman investigation with emphasis on MA vibrations was done by performing measurements in a broad frequency range (100 cm^{-1} to 3500 cm^{-1}) using three different excitation lines at 514, 785 and 1064 nm. This allowed data acquisition both at resonance (Res) as well as off-resonance conditions (Off-res). An overview of materials and excitation wavelengths is shown in the ESI (Table S2). In general, the majority of resonance Raman measurements obtained from the $MAPbX_3$ perovskites carries limited information on the vibrational properties of the materials. The main reason is that the strong absorption of the perovskites, when excited within the bandgap, can induce damage or phase transformation in the materials. This is an issue especially for $MAPbI_3$ with a phase transition from tetragonal to pseudo-cubic near room-

temperature, at 330 K. Despite keeping the laser power density very low, by working under resonance or near resonance conditions the Raman signals are frequently masked by the presence of a strong PL background signal. Furthermore, temporary PL signals which change with illumination time were observed here in Br-I mixed halide perovskites and are attributed to phase segregation, as previously reported by Hoke et al.**Error! Bookmark not defined.** (see Figure S3).

Figures 3b-d show an overview of the Raman spectra for all the perovskite films obtained under different excitation wavelengths, 1064 nm (Figure 3b), 785 nm (Figure 3c) and 514 nm (Figure 3d). In the case where the Raman features are masked by strong PL signals, the corresponding spectra are not presented. Thus, for $MAPbI_3$, we include only the spectrum obtained at 1064 nm excitation in Figure 3b, and no spectra in Figure 3c and Figure 3d, because, under near bandgap or resonance excitation, the Raman signal is either covered by a strong PL background or it is affected by the quick degradation of the sample showing spectroscopic changes during the measurement. $MAPbCl_3$ on the other hand shows no apparent change in its Raman spectrum, for all the excitation sources used. Hence, excitation at 1064 nm (Figure 3b) ensures off-resonance conditions in all cases allowing a clear and unambiguous overview of the full MA spectrum for all halide perovskite derivatives and no spectral changes were observed that could be related to humidity or light exposure of the material. Furthermore, the quality of the spectra is excellent mainly due to the fast acquisition in the FT technique and the materials tolerating high laser power densities at 1064 nm excitation, which compensate well for the inherently weaker scattering efficiency vs. the increase of the excitation wavelength (inverse fourth power law applies).

The Raman spectra reported in Figures 3b-d show a large number of MA bands which present significant changes in their spectral characteristics (shifts, widths, intensities) with halide composition. An overview of the frequencies of the measured Raman bands and their mode assignments can be found in Table 1. Almost all MA vibrational modes present a blue shift from $MAPbI_3$ towards $MAPbCl_3$ (see Figure S4) in accordance with the IR data in Ref [**Error! Bookmark not defined.**] which indicates strong NH_3−X interaction. In particular, the mode that is most sensitive to the halide content is the high frequency ν_{15}-ν_s (NH_3^+) mode which positively shifts abruptly from $MAPbI_3$ to $MAPbI_2Br$ by 33 cm^{-1} and then up to $MAPbCl_3$ by another 14 cm^{-1} Significant positive shifts also occur in all other modes related to NH_3 vibrations. This is in line with recent NMR results[53], which have shown that only the amine end of the MA group interacts strongly with the inorganic network . Nevertheless, the exact N-H bond lengths in $MAPbX_3$ cannot be accurately determined even with neutron diffraction methods due to the disorder in the MA group[53], thus the full understanding of the MA vibrational frequency shifts (e.g. the large ν_{15} shift for $MAPbI_3$ compared to the other perovskites) and the exact nature of the MA-halide interaction is not possible.

Table 1: Frequencies (in cm^{-1}) and assignments of vibrations numbered in series for MA lead derivatives MAPb[X], where [X] is the halogen composition. Modes from ν_6 and above were obtained from Raman spectra with 1064 nm excitation and are due to MA vibrations. Modes ν_3 and ν_4 were obtained from far-IR spectra. ν_1,ν_2 and ν_5 records are estimated frequencies and match well with experimental Raman spectra at low frequencies. Corresponding values for $MAPbI_3$ are shown in parenthesis to indicate that Raman experimental data are not available in this work.

Mode/[X]	I3	I2Br	IBr2	Br3	Br2Cl	BrCl2	Cl3	Assignment

ν_1	(110)	114	124	134	142	163	183	ν_s (Pb-X) this work
ν_2	(81)	85	92	99	105	121	135	ν_s (X-Pb-X) this work
ν_3	103	107	116	125	133	152	171	ν_{as} (Pb-X) this work
ν_4	65	69	72	76	82	91	114	δ_{as} (X-Pb-X) this work
ν_5	(54)	56	61	66	70	80	90	δ_s (X-Pb-X) this work
ν_6	249	264	286	323	334	460	488	τ (MA) [54,55]
ν_7	911	913	914	917	919	919	923	ρ (MA) [54,55]
ν_8	960	962	965	968	971	974	977	ν (C-N) [55]
ν_9	1247	1246	1247	1248	1249	1248	1249	ρ (MA) [30]
ν_{10}	1424	1423	1425	1428	1427	1426	1430	δ_s (CH_3) [55]
ν_{11}	1444	1444	1451	1450	1451	1453	1454	δ_{as} (CH_3) [55]
ν_{12}	1469	1472	1475	1478	1480	1483	1483	δ_s (NH_3^+) [30]
ν_{13}	1580	1581	1584	1587	1588	1593	1592	δ_{as} (NH_3^+) [30]
-	2706	2712	2716	2714	2715	2717	2719	combination modes [30]
-	2821	2823	2824	2827	2827	2829	2830	combination modes [30]
-	2906	2906	2845	2846	2845	2847	2848	combination modes [30]
ν_{14}	2959	2961	2963	2966	2968	2969	2972	ν_{as} (CH_3) [30]
ν_{15}	2993	3026	3030	3035	3036	3036	3040	ν_s (NH_3^+) [55]

ν: stretching; δ: bending; ρ: rocking; τ: torsion; s:symmetric; as:asymmetric

Characteristic internal vibrational modes of MA appear at high frequencies, just below 1000 cm^{-1} (C-N stretching), at 1400 cm^{-1} to 1600 cm^{-1} (CH_3 and NH_3 bending) and at around 3000 cm^{-1} (CH_3 and NH_3 stretching) and are well studied for methylammonium halides[30,55]. The most interesting vibrational modes are the rocking vibration, ν_7, and low-frequency torsion, ν_6, of MA around the C-N axis. The MA rocking mode, ν_7, appears in between 911 cm^{-1} to 923 cm^{-1} and sharpens, increases in intensity and red-shifts when moving towards heavier halides

Cl→Br→I (Figure 3b-d, Figure S4); the same trend was found for other modes (e.g., the ν_{12}, $\delta_s(NH_3^+)$ mode). This behavior can be attributed to orientational ordering of MA for which ν_7, having the E symmetry[56], is a good indicator. The effect can be analyzed by the calculation of the correlation times (τ_c) from the peak full width at half maximum (FWHM)[29], which are shown in Figure 4a, according to eq. 2:

$$\tau_c = \frac{1}{2\pi\, c\, \mathrm{FWHM}} \qquad (2)$$

where c is the velocity of light.

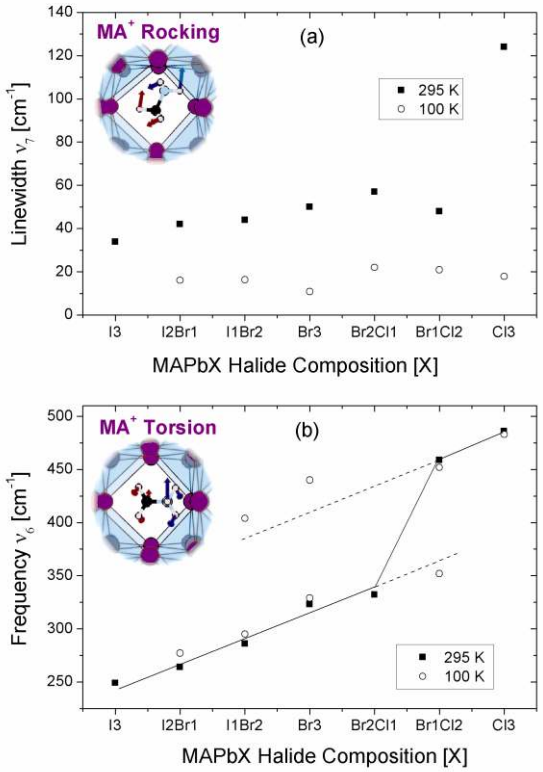

Figure 4: **(a)** FWHM of the ν_7 rocking mode averaged over measurements obtained at RT with different laser lines (solid squares – standard deviation < 5 cm^{-1}) as well as at LT (100 K) obtained at 785 nm excitation (open circles) **(b)** Raman frequency of the torsional mode averaged over measurements obtained at RT with different laser lines (solid squares standard

deviation < 3 cm^{-1}) and corresponding results at LT (100 K) obtained at 785 nm (open circles). Solid line guides the eye for halogen dependence of the RT data and is extrapolated either sides with dashed lines.

The results show correlation times below 0.15 ps for the ν_7 rocking vibration for all perovskite derivatives. τ_c gradually decreases from 0.15 ps to 0.1 ps from $MAPbI_3$ up to $MAPbBrCl_2$ and drops to 0.05 ps for $MAPbCl_3$. Measurements of MA rocking vibration dynamics can be compared with early IR absorption data[29] obtained from large perovskite crystals, where the trend of correlation time decrease from heavy to light halides is also followed, as well as with recent results on very high quality thin films prepared with the dual source evaporation method. In both these literature works, the τ_c values for $MAPbI_3$were substantially larger. Thus, the shorter correlation time in our samples is attributed to their polycrystalline character.

The ν_6 mode mainly consists of an NH_3 motion and has an A_2 symmetry which makes it forbidden in IR but permitted in Raman[55]. This mode is easily accessed in all Raman experiments and is analyzed in a straightforward way as it is not overlapping with other modes. For $MAPbCl_3$[54] the mode is observed at 488 cm^{-1} and presents an extremely large red frequency shift upon halide substitution, moving down to 249 cm^{-1} for $MAPbI_3$ (see Figure 4b and Table 1). This large spread of resonance frequencies for MA is unusual for a torsional mode and indicates intense MA deformation and a strong interaction of MA with the inorganic cage. Fitting of ν_6 for different halide derivatives gives a continuous shift from $MAPbI_3$ to $MAPbBr_2Cl$, but jumps to higher wavenumbers for perovskites with large amounts of Cl, as shown in Figure 4b. According to recent theoretical studies[23], different mechanisms like molecular deformation and dipolar orientational ordering of the MA as well as strength of the NH_3-X interaction are strongly

affected by the nature of the halide in the perovskite, and result in large shifts in the frequency of the MA torsion. Among them, changes in NH_3-X interaction upon halide substitution is the most prominent reason for the large frequency shift of the ν_6 mode, considering that it affects the frequencies of all other MA modes, too, in the same manner, even though to a much lesser extent. Preliminary calculations performed with the same methodology reported by Brivio at al.[38] confirm the observed increase of the torsional mode frequency for perovskites with Br and Cl with respect to iodine. This is due to a halide specific NH_3−X interaction, and to a confinement effect. In fact, lighter halide results in a smaller cavity inside the inorganic cage that uplifts the frequencies of the molecular modes, and reduces the distance between hydrogen and halide, amplifying the resulting shift. In Figure S5 we attempt a correlation of the torsional mode peak frequency at room-temperature (RT) against the measured band gap for the various perovskite halides. Halide substitution results in vast changes of the materials optical properties, which can significantly affect their vibrational frequencies as also proposed before[30] by correlating the red shifts of MA vibrations in the Cl→Br→I order to the increase in the polarizability of the dielectric medium (Lorentz-Lorenz shift).

Interestingly, the signal intensity of ν_6 is much stronger for single halide perovskites (see Figure 3b-d) and its linewidth is not very broad, ranging from 40 to 60 cm^{-1}. In the mixed halide perovskites a big drop in the ν_6 intensity takes place which goes along with extensive linewidth broadening, reaching values up to 150 cm^{-1}. A general peak broadening can be caused in several ways. A decrease in long-range order and crystallinity typically yields broader peaks. Unresolved mode-splitting also causes an increase of peak width and is connected to possible asymmetries of the mode. Such mode splitting can be enhanced by micro-structural inhomogenities due to an uneven distribution of a halide in the perovskite. This effect has been reported before for

$MAPbI_{3-x}Br_x$, which forms micro-domains upon crystallization that transform into a single-phase within a few weeks[57] but also segregates again upon illumination[12].

The informative torsional and rocking vibrations were further examined by comparative low-temperature Raman measurements in order to elucidate their behavior by lowering the symmetry of the perovskite structure.

3.4 LOW TEMPERATURE RAMAN MEASUREMENTS

Another series of Raman experiments was performed for all perovskites at 100 K which is well below the phase transition of all materials into the orthorhombic phase[46]. Characteristic reduced spectra at low temperature are shown in Figure 5a obtained with excitation at 785 nm. The inset shows off-resonance spectra of $MAPbBrCl_2$ and $MAPbCl_3$ using 514 nm excitation. Peak frequencies of the strongest MA vibrations are given in Table S3. Mode splitting of the low-frequency modes was observed due to the lowering of the crystal symmetry. All materials transform from tetragonal to orthorhombic in the temperature range of 148.8-171.5 K[58]. Splitting was more evident for lighter halide derivatives, in accordance to early results for $MAPbCl_3$[54]. In the case of heavier derivatives, mode splitting was only partially observed due to the shifting of the majority of the modes below the experimentally accessed frequency range. Furthermore, apart from narrowing and blue shifting of the MA high frequency bands above 950 cm^{-1}, no clear MA mode splitting was evidenced upon decrease of the temperature. A similar effect has been reported before for mid-IR data below the phase transition temperature[29] as well as for Raman in other perovskite systems[59] implying that the crystal deformation does not drastically affect the high frequency vibrations of the MA units.

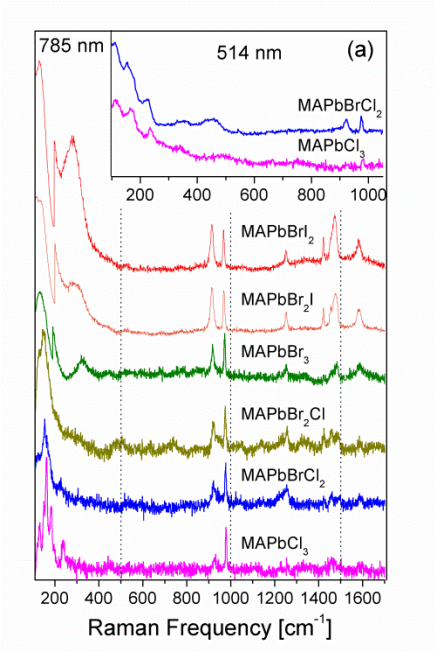

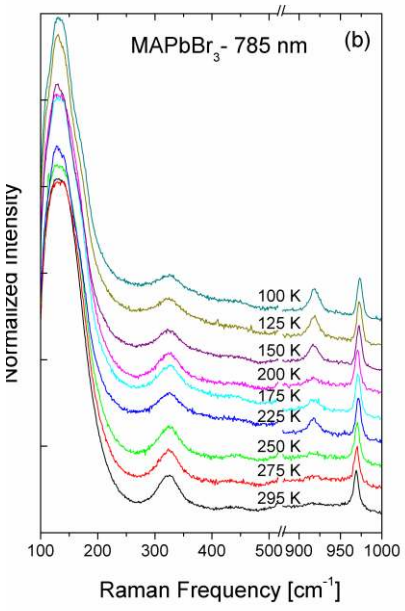

Figure 5: **(a)** Raman measurements of $MAPbX_{3-x}Y_x$ perovskites at 100 K obtained with 785 nm excitation. Intensity of the top three spectra below 200 cm^{-1} is scaled down by 3 for better vision of the spectra. Inset shows spectra obtained with 514 nm excitation. **(b)** Raman spectra of $MAPbBr_3$ (785 nm) vs. temperature variation from 100 K (LT) to 295 K (RT).

It is remarkable that at LT the rocking vibrations ν_7 and ν_9 at 920 and 1250 cm^{-1} present considerable linewidth narrowing. Thus, the ν_7 rocking mode width decreases to about 20 cm^{-1} for all perovskite derivatives (see Figure 4a) and the ν_7 correlation time increases from below 0.15 ps at RT to above 0.25 ps at 100 K, which implies MA dipolar ordering[29], in accordance with quasi-elastic neutron scattering results[22].

Further insight into the behavior of the ν_6 torsion mode can be extracted from the low-temperature (LT) data. While the measurements at RT showed a jump to higher wavenumbers for the $MAPbBrCl_2$ and $MAPbCl_3$ perovskites, at LT pairs of peaks appeared (see spectra in Figure 5a and analysis in Figure 4b) that line up with modes on either side of the gap, suggesting that those peaks in fact represent two distinctive vibrational bands. The appearance of two torsional bands at low-temperature is in line with early studies for $MAPCl_3$[54]. Doubling of the torsional modes for the low symmetry orthorhombic phase and linewidth broadening might be due to different NH_3-X bonding schemes of the organic molecule within the hybrid[60]. On the other hand, the frequencies of the torsional modes at low temperature show small, mostly blue shifts relative to those at RT.

Another important aspect of the torsional mode is its significant broadening in the orthorhombic phase. The unit cell of this phase contains four different MA units and according to our preliminary calculations, the frequencies of respective modes are split in four due to slightly different local environments. This split is in the order of few cm^{-1} and therefore too small to be resolved but contributes in significant linewidth broadening. Moreover, as proved and observed in molecules[61,62] or complex structures[63], Van-der-Waals forces that are enhanced at low temperature, affect the stiffness of the bonds and influence the non-harmonic terms of the vibration that lead to a larger broadening of the peak. This effect strongly depends on the

position and the geometry of the system and could justify the different behavior below the transition temperature. In previous work[64] it has been reported an anomalous temperature behavior of a low frequency Raman peak in NH_4Br around phase transition. This anomaly results in asymmetric peak shape and anomalous broadening of the signal. These effects are addressed and explained with a long range order of the NH_4 cations. We can imagine that a similar mechanism, regarding the MA ordering, could influence the linewidths at LT of the torsional mode in the perovskite halides too.

In addition to fixed LT measurements at 100 K, variable temperature Raman measurements from 295 K to 100 K have been carried out for $MAPbBr_3$. During this temperature ramp the material was transformed progressively from cubic to the tetragonal I phase (236.3 K), the tetragonal II phase at 154.0 K and the orthorhombic phase at 148.8 K[46]. Recorded Raman spectra are shown in Figure 5b. $MAPbBr_3$ was chosen as the intermediate representative of our halide series and because of its high purity (see XRD in Figure S1), the fact that the full temperature dependence has not been reported before in the literature ($MAPbCl_3$ has been studied in ref. [**Error! Bookmark not defined.**] and $MAPbI_3$ Raman signal is covered by a strong PL background at 785 nm excitation) and its significance as light absorber for the preparation of very stable perovskite solar cells[8-11,65].

All high frequency MA modes above 950 cm^{-1} present a 'normal' behavior with line narrowing and blue shift upon temperature decrease. Important observations are made by following the temperature dependence of the spectra below 950 cm^{-1} where peculiar behavior of the MA torsional and rocking modes at 320 cm^{-1} and 925 cm^{-1} are observed upon moving from the cubic (295 K) to the orthorhombic phase (100 K).

Figure 6 plots the temperature dependence of the linewidths for the 'abnormal' torsional ν_6 and rocking ν_7 modes in comparison to the CN stretching ν_8 mode which shows a 'normal' behavior. The slope of linewidth against temperature shows a change for ν_7, at about 175 K, slightly above the tetragonal I-II phase transition at 154 K. This transition temperature is close to the temperature of a discontinuous decrease of the real part of the dielectric permittivity[58] as well as of significant changes in the H^1-NMR spectra and relaxation time[66]. According to this early H^1-NMR result, the tetragonal I to tetragonal II phase transition affects the alignment of MA with freezing of the C-N axis.

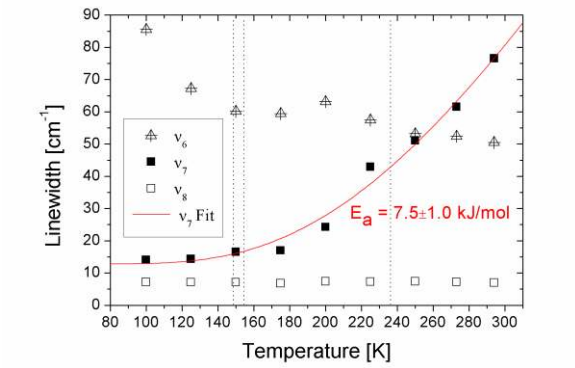

Fig. 6 Temperature dependence of linewidths for the torsional ν_6, rocking ν_7 and CN stretching ν_8 vibrations of $MAPbBr_3$. Solid line represent fitting of ν_7 linewidths by eq. 1 with b=0. Dotted lines mark temperatures of phase transitions.

The temperature dependence of the linewidth of the ν_7 rocking mode in Figure 6, was used to calculate the activation energy (E_a) of the order-disorder process, according to equation (3)[67-69].

$$FWHM(T) = a + bT + c\,exp(-Ea / RT) \qquad (3)$$

where a, b, c are fitting parameters and R is the gas constant. The linear term describes the anharmonicity factor and the exponential term the increase of the linewidth due to the thermal reorientational motions. We fitted the FWHM(T) data of ν_7 in Figure 6 with eq. (3), neglecting the linear term which has a small contribution and ended up with an estimation of the activation energy of E_a = 7.5±1.0 kJ/mol which resembles the energy barrier in the disorder of the MA units. This value is very similar to that found for the rocking vibration of NH_3 in $[Mn(NH_3)_6](ClO_4)_2$[Error! Bookmark not defined.]. As shown in Figure 6, the reorientational motions are not significantly disturbed near the phase transition temperature which is indicative that the order-disorder of the organic molecule does not contribute significantly in the phase transition mechanism[69]. Among different vibrational modes, the main torsional mode at about 320 cm^{-1} is the only one that shows line broadening instead of narrowing upon decreasing the temperature (see Figure 6). This broadening occurs progressively but shows a steep rise below the transition to the orthorhombic phase. This interesting behavior, which was also observed for other perovskite halides as discussed before, can be justified by the emergence of new unresolved torsional bands and long range MA order in the low symmetry phase.

4. CONCLUSIONS

In summary, our study gives a complete overview of the vibrational properties of single and mixed $MAPbX_3$ (X = Cl, Br, I) perovskites. Measurement in off-resonance conditions, at room- and low-temperatures, and a comparison of the Raman with far-IR spectra allow an unambiguous attribution of inorganic and organic modes and their shifts against halide constitution and temperature. Using three different excitation wavelengths for the Raman measurements, a significant influence of beam-induced degradation on the spectra of this material class can be ruled out for the first time in the literature. The low frequency range is dominated by the modes

of the inorganic anion and the frequency shifts versus halide content is governed by the Pb-X reduced mass. Insight into structural dynamics of the MA cation has been given where specific vibrations such as the NH_3 rocking mode indicate ordering of MA at low temperatures. Amongst different modes, the MA torsion is particularly interesting since it spans a broad frequency range from 249 cm^{-1} to 488 cm^{-1} by altering the halogen content. This behavior is attributed to changes in the interaction between the NH_3 head of MA and the halide. Furthermore, the MA torsional band shows broadening and splitting at 100 K in the orthorhombic phase, which indicates possible different MA-X bonding schemes. We hope that these findings encourage a broader usage of vibrational spectroscopy for inorganic-organic hybrid perovskites, and aid a better understanding of their properties, which rank them among the most efficient solar cell active materials.

ASSOCIATED CONTENT

Supporting Information Available: Table S1: Lattice parameters from XRD data for $MAPbX_3$ perovskites; Table S2: Band gaps and laser excitation energies for the Raman and PL investigation of perovskite materials; Table S3: Overview of main MA Raman frequency peaks above 900 cm^{-1}, measured at 100 K.

Figure S1: Full powder XRD patterns of all halide perovkites; Figure S2: Fitting analysis of the far-IR absorption spectra; Figure S3: Spectra showing shifting of PL during measuring $MAPbI_2Br$ under resonance (514 nm) excitation, indicating phase segregation; Figure S4: Raman frequency shifts of strongest MA modes above 900 cm^{-1} for various halogen contents in $MAPbX_3$; Figure S5: The frequency of the ν_6 torsional mode at RT against the band gaps for all measured $MAPbX_3$ derivatives.

This information is available free of charge via the internet at at http://pubs.acs.org<http://pubs.acs.org/>

AUTHOR INFORMATION

Corresponding Author

* Athanassios G. Kontos, INN-NCSR Demokritos, 15310 Athens, GR; Tel: +30 210 6503668; Fax: +30 210 6511766; e-mail: a.kontos@inn.demokritos.gr

Author Contributions

The manuscript was written through contributions of all authors. All authors have given approval to the final version of the manuscript. ‡These authors contributed equally.

ACKNOWLEDGMENT

We acknowledge Dr. George Kordas for providing the 50 cm^{-1} NIR filter for the low frequency Raman measurements and Dr. Eirini Siranidi for her assistance in Raman spectra acquisition. For enlightening and amicable conversations we would like to thank Dr. Jarvist Frost and Harry Georgiou. This project is funded through the EU DESTINY Network (Grant 316494).

REFERENCES

[1]Kojima, A.; Teshima, K.; Shirai, Y.; Miyasaka, T. Organometal Halide Perovskites as Visible-Light Sensitizers for Photovoltaic Cells. *J. Am. Chem. Soc.* **2009,** *131,* 6050–6051.

[2] Im, J.-H.; Lee, C.-R.; Lee, J.-W.; Park, S.-W.; Park, N.-G. 6.5% Efficient Perovskite Quantum-Dot-Sensitized Solar Cell. *Nanoscale* **2011,** *3,* 4088–4093.

[3] Kim, H.-S.; Lee, C.-R.; Im, J.-H.; Lee, K.-B.; Moehl, T.; Marchioro, A.; Moon, S.-J.; Humphry-Baker, R.; Yum, J.-H.; Moser, J. E.; et. al. Lead Iodide Perovskite Sensitized All-

Solid-State Submicron Thin Film Mesoscopic Solar Cell with Efficiency Exceeding 9%. *Sci. Rep.* **2012,** *2,* 591.

[4] Lee, M. M.; Teuscher, J.; Miyasaka, T.; Murakami, T. N.; Snaith, H. J. Efficient Hybrid Solar Cells Based on Meso-Superstructured Organometal Halide Perovskites. *Science* **2012,** *338,* 643–647.

[5] Zhang, W.; Saliba, M.; Moore, D. T.; Pathak, S. K.; T. Hörantner, M. T.; Stergiopoulos, T.; Stranks, S. D.; Eperon, G. E.; Alexander-Webber, J. A.; Abate, A.; et al. Ultrasmooth organic–inorganic perovskite thin-film formation and crystallization for efficient planar heterojunction solar cells. *Nat. Commun.* **2015,** *6,* 6142.

[6] Park, B.; Philippe, B.; Jain, S. M.; Zhang, X.; Edvinsson, T.; Rensmo, H.; Zietz, B.; Boschloo, G. Chemical engineering of methylammonium lead iodide/bromide perovskites: tuning of optoelectronic properties and photovoltaic performance. *J. Mater. Chem. A* **2015,** *3,* 21760-21771.

[7] http://www.solarserver.com/solar-magazine/solar-news/current/2015/kw50/epfl-achieves-21-world-record-efficiency-for-perovskite-solar-pv-cells.html (accessed December, 21, 2015)

[8] Noh, J. H.; Im, S. H.; Heo, J. H.; Mandal, T. N.; Seok, S. Il. Chemical Management for Colorful, Efficient, and Stable Inorganic-Organic Hybrid Nanostructured Solar Cells. *Nano Lett.* **2013,** *13,* 1764–1769.

[9] Conings, B.; Drijkoningen, J.; Gauquelin, N.; Babayigit, A.; D'Haen, J.; D'Olieslaeger, L.; Ethirajan, A.; Verbeeck, J.; Manca, J.; Mosconi, E.; De Angelis, F.; et. al. Intrinsic Thermal Instability of Methylammonium Lead Trihalide Perovskite. *Adv. Energy Mater.* **2015,** 1500477.

[10] Zhang, Y.-Y.; Chen, S.; Xu, P.; Xiang, H.; Gong, X.-G.; Walsh, A.; Wei, S.-H. Intrinsic Instability of the Hybrid Halide Perovskite Semiconductor $CH_3NH_3PbI_3$. *arXiv Prepr.* **2015,** arXiv:1506.01301.

[11] Buin, A.; Comin, R.; Xu, J.; Ip, A. H.; Sargent, E. H. Halide-Dependent Electronic Structure of Organolead Perovskite Materials. *Chem. Mater.* **2015,** *27,* 4405–4412.

[12] Hoke, E. T.; Slotcavage, D. J.; Dohner, E. R.; Bowring, A. R.; Karunadasa, H. I.; McGehee, M. D. Reversible Photo-Induced Trap Formation in Mixed-Halide Hybrid Perovskites for Photovoltaics. *Chem. Sci.* **2015,** *6,* 613–617.

[13] Stranks, S. D.; Eperon, G. E.; Grancini, G.; Menelaou, C.; Alcocer, M. J. P.; Leijtens, T.; Herz, L. M.; Petrozza, A.; Snaith, H. J. Electron-Hole Diffusion Lengths Exceeding 1 Micrometer in an Organometal Trihalide Perovskite Absorber. *Science* 2013, 342, 341–344.

[14] Colella, S.; Mosconi, E.; Fedeli, P.; Listorti, A.; Gazza, F.; Orlandi, F.; Ferro, P.; Besagni, T.; Rizzo, A.; Calestani, G.; et. al. $MAPbI_{3-x}Cl_x$ Mixed Halide Perovskite for Hybrid Solar Cells : The Role of Chloride as Dopant on the Transport and Structural Properties. *Chem. Mater.* **2013,** *25,* 4613–4618.

[15] Colella, S.; Mosconi, E.; Pellegrino, G.; Alberti, A.; Guerra, V. L. P.; Masi S.; Listorti, A.; Rizzo, A.; Condorelli, G. G.; De Angelis, F.; et. al. Elusive Presence of Chloride in Mixed Halide Perovskite Solar Cells. *J. Phys. Chem. Lett.* **2014,** *5,* 3532–3538.

[16] Starr, D. E.; Sadoughi, G.; Handick, E.; Wilks, R. G.; Alsmeier, J. H.; Köhler, L.; Gorgoi, M.; Snaith, H. J.; Bär, M. Direct Observation of an Inhomogeneous Chlorine Distribution in $CH_3NH_3PbI_{3-x}Cl_x$ Layers: Surface Depletion and Interface Enrichment. *Energy Environ. Sci.* **2015,** *8,* 1609–1615.

[17] Milot, R. L.; Eperon, G. E.; Snaith, H. J.; Johnston, M. B.; Herz, L. M. *Temperature-Dependent Charge-Carrier Dynamics in $CH_3NH_3PbI_3$ Perovskite Thin Films. Adv. Funct. Mater.* **2015,** *25,* 6218-6227.

[18] Weber, D. $CH_3NH_3PbX_3$, a Pb(II)-System with Cubic Perovskite Structure. *Zeitschrift für Naturforsch.* **1978,** *33b,* 1443–1445.

[19] Poglitsch, A.; Weber, D. Dynamic Disorder in Methylammoniumtrihalogenoplumbates (II) Observed by Millimeter-Wave Spectroscopy. *J. Chem Phys.* **1987,** *87,* 6373-6378.

[20] Wasylishen, R. E.; Knop, O.; Macdonald, J. B. Cation Rotation in Methylammonium Lead Halides. *Solid State Commun.* **1985,** *56,* 581–582.

[21] Weller, M. T.; Weber, O. J.; Henry, P. F.; Di Pumpo, A. M.; Hansen, T. C. Complete Structure and Cation Orientation in the Perovskite Photovoltaic Methylammonium Lead Iodide between 100 and 352 K. *Chem. Commun.* **2015,** *51,* 4180–4183.

[22] Leguy, A. M. A.; Frost, J. M.; McMahon, A. P.; Sakai, V. G.; Kochelmann, W.; Law, C.; Li, X.; Foglia, F.; Walsh, A.; O'Regan, B. C.; et. al. The Dynamics of Methylammonium Ions in Hybrid Organic-Inorganic Perovskite Solar Cells. *Nat. Commun.* **2015,** *6,* 7124.

[23] Quarti, C.; Grancini, G.; Mosconi, E.; Bruno, P.; Ball, J. M.; Lee, M. M.; Snaith, H. J.; Petrozza, A.; De Angelis, F. The Raman Spectrum of the CH3NH3PbI3 Hybrid Perovskite: Interplay of Theory and Experiment. *J. Phys. Chem Lett.* **2014,** *5,* 279–284.

[24] Frost, J.; Butler, K.; Brivio, F. Atomistic Origins of High-Performance in Hybrid Halide Perovskite Solar Cells. *Nano Lett.* **2014,** *14,* 2584–2590.

[25] Liu, S.; Zheng, F.; Koocher, N. Z.; Takenaka, H.; Wang, F.; Rappe, A. M. Ferroelectric Domain Wall Induced Band Gap Reduction and Charge Separation in Organometal Halide Perovskites. *J. Phys. Chem. Lett.* **2015,** *6,* 693–699.

[26] Leguy, A.; Azarhoosh, P.; Alonso, M. I.; Campoy-Quiles, M.; Weber, O. J.; Yao, J.; Bryant, D.; Weller, M. T.; Nelson, J.; Walsh, A.; et. al. Experimental and Theoretical Optical Properties of Methylammonium Lead Halide Perovskites. *Nanoscale* **2015,** DOI: 10.1039/C5NR05435D.

[27] Quarti, C.; Mosconi, E.; De Angelis, F. Interplay of Orientational Order and Electronic Structure in Methylammonium Lead Iodide: Implications for Solar Cells Operation. *Chem. Mater.* **2014,** *26,* 6557–6569.

[28] Wu, B.; Fu, K.; Yantara, N.; Xing, G.; Sun, S.; Sum, T. C.; Mathews, N. Charge Accumulation and Hysteresis in Perovskite-Based Solar Cells: An Electro-Optical Analysis. *Adv. Energy Mater.* **2015,** 1500829.

[29] Onoda-Yamamuro, N.; Matsuo, T.; Suga, H. Calorimetric and IR Spectroscopic Studies of Phase Transitions in Methylammonium Trihalogenoplumbates. *J. Phys. Chem. Solids* **1990,** *51,* 1383–1395.

[30] Glaser, T.; Muller, C.; Sendner, M.; Krekeler, C.; Semonin, O. E.; Hull, T. D.; Yaffe, O.; Owen, J. S.; Kowalsky, W.; Pucci, A.; et. al. Infrared Spectroscopic Study of Vibrational Modes in Methylammonium Lead Halide Perovskites. *J. Phys. Chem Lett.* **2015,** *6,* 2913–2918.

[31] Bakulin, A. A.; Selig, O.; Bakker, H. J.; Rezus, Y. L. A.; Müller, C.; Glaser, T.; Lovrincic, R.; Sun, Z.; Chen, Z.; Walsh, A.; et. al. Real-Time Observation of Organic Cation Reorientation in Methylammonium Lead Iodide Perovskites. *J. Phys. Chem. Lett.* **2015,** *6,* 3663–3669.

[32] Müller, C.; Glaser, T.;Plogmeyer, M.; Sendner, M.; Döring, S.; Bakulin, A.A.; Brzuska, C.; Scheer, R.; Pshenichnikov, M.S.; Kowalsky, W.; et. al. Water Infiltration in Methylammonium Lead Iodide Perovskite: Fast and Inconspicuous. *Chem. Mater.* **2015,** *27,* 7835–7841.

[33] Mosconi, E.; Quarti, C.; Ivanovska, T.; Ruani, G.; De Angelis, F. Structural and Electronic Properties of Organo-Halide Lead Perovskites: A Combined IR-Spectroscopy and Ab Initio Molecular Dynamics Investigation. *Phys. Chem. Chem Phys.* **2014,** *16,* 16137–16144.

[34] Perez-Osorio, M. A.; Milot, R. L.; Filip, M. R.; Patel, J. B.; Herz, L. M.; Johnston, M. B.; Giustino, F. Vibrational Properties of the Organic-Inorganic Halide Perovskite $CH_3NH_3PbI_3$ from Theory and Experiment: Factor Group Analysis, First-Principles Calculations, and Low-Temperature Infrared Spectra. J. Phys. Chem. C **2015,** *119,* 25703–25718.

[35] Grancini, G.; Marras, S.; Prato, M.; Giannini, C.; Quarti, C.; De Angelis, F.; Bastiani, M. De; Eperon, G. E.; Snaith, H. J.; Manna, L.; et. al. The Impact of the Crystallization Processes on the Structural and Optical Properties of Hybrid Perovskite Films for Photovoltaics. *J. Phys. Chem Lett.* **2014,** *5,* 3836–3842.

[36] Ledinsky, M.; Löper, P.; Niesen, B.; Holovsky, J.; Moon, S. J.;Yum, J. H.; De Wolf, S.; Fejfar, A.; Ballif, C. Raman Spectroscopy of Organic-Inorganic Halide Perovskites. *J. Phys. Chem. Lett.* **2015,** *6,* 401–406.

[37] Park, B.; Jain, S. M.; Zhang, X.; Hagfeldt, A.; Boschloo, G.; Edvinsson, T. Resonance Raman and Excitation Energy Dependent Charge Transfer Mechanism in Halide-Substituted Hybrid Perovskite Solar Cells. *ACS Nano* **2015,** *9,* 2088–2101.

[38] Brivio, F.; Frost, J. M.; Skelton, J. M.; Jackson, A. J.; Weber, O. J.; Weller, M. T.; Walsh, A.; Goni, A. R.; Leguy, A. M. A.; Barnes, P. R. F.; et. al. Lattice Dynamics and Vibrational Spectra of the Orthorhombic, Tetragonal and Cubic Phases of Methylammonium Lead Iodide. *Phys. Rev. B* **2015,** *92,* 144308.

[39] Gottesman, R.; Gouda, L.; Kalanoor, B. S.; Haltzi, E.; Tirosh, S.; Rosh-Hodesh, E.; Tischler, Y.; Zaban, A.; Quarti, C.; Mosconi, E.; et.al. Photoinduced Reversible Structural Transformations in Free-Standing $CH_3NH_3PbI_3$ Perovskite Films. *J. Phys. Chem Lett.* **2015,** *6,* 2332–2338.

[40] Leijtens, T.; Hoke, E. T.; Grancini, G.; Slotcavage, D. J.; Eperon, G. E.; Ball, J. M.; De Bastiani, M.; Bowring, A. R.; Martino, N.; Wojciechowski, K.; et. al. Mapping Electric Field-Induced Switchable Poling and Structural Degradation in Hybrid Lead Halide Perovskite Thin Films. *Adv. Energy Mater.* **2015,** *5,* 1500962.

[41] Antoniadou, M.; Siranidi, E.; Vaenas, N.; Kontos, A. G.; Stathatos, E.; Falaras, P. Photovoltaic Performance and Stability of $CH_3NH_3PbI_{3-x}Cl_x$ Perovskites. *J. Surfaces Interfaces Mater.* **2014,** *2,* 323–327.

[42] Misra, R. K.; Aharon, S.; Li, B.; Mogilyansky, D.; Visoly-Fisher, I.; Etgar, L.; Katz, E. A. Temperature- and Component-Dependent Degradation of Perovskite Photovoltaic Materials under Concentrated Sunlight. *J. Phys. Chem. Lett.* **2015,** *6,* 326–330.

[43] Kedem, N.; Brenner, T. M.; Kulbak, M.; Schaefer, N.; Levcenko, S.; Levine, I.; Abou-Ras, D.; Hodes, G.; Cahen, D. Light-Induced Increase of Electron Diffusion Length in a P-N Junction Type $CH_3NH_3PbBr_3$ Perovskite Solar Cell. *J. Phys. Chem Lett.* **2015,** *6,* 2469–2476.

[44] Larson, A. C.; von Dreele, R. B. General Structure Analysis System; Rep. LAUR 85-748; Los Alamos Lab. 1994.

[45] Kamitsos, E. I.; Kapoutsis, J. A.; Jain, H.; Hsieh, C. H. Vibrational Study of the Role of Trivalent Ions in Sodium Trisilicate Glass. *J. Non. Cryst. Solids* **1994,** *171,* 31–45.

[46] Onoda-Yamamuro, N.; Yamamuro, O.; Matsuo, T.; Suga, H. *P*-T Phase Relations of $CH_3NH_3PbX_3$ (X=Cl, Br, I) Crystals. *J. Phys. Chem. Solids* **1992,** *53,* 277–281.

[47] Stoumpos, C. C.; Malliakas, C. D.; Kanatzidis, M. G. Semiconducting Tin and Lead Iodide Perovskites with Organic Cations: Phase Transitions, High Mobilities, and near-Infrared Photoluminescent Properties. *Inorg. Chem.* **2013,** *52,* 9019–9038.

[48] Choi, J. J.; Yang, X.; Norman, Z. M.; Billinge, S. J. L.; Owen, J. S. Structure of Methylammonium Lead Iodide Within Mesoporous Titanium Dioxide: Active Material in High Performance Perovskite Solar Cells. *Nano Lett.* **2013,** *14,* 127–133.

[49] Wei, M.; Chung, Y.-H.; Xiao, Y.; Chen, Z. Color Tunable Halide Perovskite $CH_3NH_3PbBr_{3-x}Cl_x$ Emission via Annealing. *Org. Electron.* **2015,** *26,* 260–264.

[50] Wehrenfennig, C. Ultrafast Spectroscopy of Charge Separation, Transport and Recombination Processes in Functional Materials for Thin-Film Photovoltaics, PhD Thesis, Oxford University, 2014.

[51] Kitazawa, N.; Watanabe, Y.; Nakamura, Y. Optical Properties of $CH_3NH_3PbX_3$ (X = Halogen) and Their Mixed-Halide Crystals. *J. Mater. Sci.* **2002,** *37,* 3585–3587.

[52] Nakamoto, K. in Infrared and Raman Spectra of Inorganic and Coordination Compounds, Part A, Theory and Applications in Inorganic Chemistry, 6th Edition; Wiley, 2009.

[53] Baikie, T.; Barrow, N. S.; Fang, Y.; Keenan, P. J.; Slater, P. R.; Piltz, R. O.; Gutmann, M.; Mhaisalkar, S. G.; White, T. J. A Combined Single Crystal neutron/X-Ray Diffraction and Solid-State Nuclear Magnetic Resonance Study of the Hybrid Perovskites $CH_3NH_3PbX_3$ (X = I, Br and Cl). *J. Mater. Chem. A* **2015,** *3,* 9298–9307.

[54] Maalej, A.; Abid, A.; Kallel, A.; Daoud, A.; Lautie, A.; Romain, F. Phase Transitions and Crystal Dynamics in the Cubic Perovskite $CH_3NH_3PbCl_3$. *Solid State Commun.* **1997,** *103,* 279-284.

[55] Theoret, A.; Sandorfy, C. The Infrared Spectra of Solid Methylammonium Halides-II. *Spectrochim. Acta* **1967,** *23A,* 519–542.

[56] Matsuo, T.; Ueda, M.; Suga, H. Calorimetric and Spectroscopic Studies of the Critical Phase Transition in $(CH_3NH_3)_2[SnCl_6]$. *Chem. Phys. Lett.* **1981,** *82,* 577–580.

[57] Sadhanala, A.; Deschler, F.; Thomas, T. H.; Dutton, E.; Goedel, K. C.; Hanusch, F. C.; Lai, M. L.; Steiner, U.; Bein, T.; Docampo, P.; et. al. Preparation of Single-Phase Films of $CH_3NH_3Pb(I_{1-x}Br_x)_3$ with Sharp Optical Band Edges. *J. Phys. Chem Lett.* **2014,** *5,* 2501–2505.

[58] Onoda-Yamamuro, N.; Matsuo T.; Duga H. Dielectric Study of CH3NH3PbX3 (X = Cl, Br, I). *J. Phys. Chem. Solids* **1992,** *53,* 935-939.

[59] Popović, Z. V; Kontos, A. G.; Raptis, Y. S.; Isobe, M.; Ueda, Y. Raman Scattering Study of β-Sr(0.33)V(2)O(5) in Charge Disordered and Ordered Phase. *J. Phys.: Condens. Matter* **2006,** *18,* 7779–7787.

[60] Mitzi, D. B. Templating and Structural Engineering in Organic–inorganic Perovskites. *J. Chem. Soc. Dalt. Trans.* **2001,** *1,* 1–12.

[61] Michels, J. P. J.; Schouten, J. A. Broadening of Vibrational Raman Spectra by Concentration Fluctuations: A Molecular Dynamics Survey. *Int. J. Thermophys.* **2001,** *22,* 339–355.

[62] Das, A.; Kumar, K., Raman Anisotropic Linewidth Dependence on the Van Der Waals Volume of the Interacting Systems. *J. Raman Spectrosc.* **1999,** *30,* 547–549.

[63] Rao, A. M.; Chen, J.; Richter, E.; Schlecht, U.; Eklund, P. C.; Haddon, R. C.; Venkateswaran, U. D.; Kwon, Y. K.; Tománek, D. Effect of van Der Waals Interactions on the Raman Modes in Single Walled Carbon Nanotubes. *Phys. Rev. Lett.* **2001,** *86,* 3895–3898.

[64] Wang, C. H.; Wright, R. B., Nature of the λ Transition and the 56 cm^{-1} Anomalous Raman Mode in Ammonium Bromide. *J. Chem Phys.* **1972,** *57,* 4401.

[65] Jeon, N. J.; Noh, J. H.; Yang, W. S.; Kim, Y. C.; Ryu, S.; Seo, J.; Seok, S. Il. Compositional Engineering of Perovskite Materials for High-Performance Solar Cells. *Nature* **2015,** *517,* 476–480.

[66] Knop, O.; Wasylishen, R. E.; White, M. A.; Cameron, T. S.; Van Oort, M. J. M. Alkylammonium lead halides. Part 2. $CH_3NH_3PbX_3$ (X = Cl, Br, I) Perovskites: Cuboctahedral Halide Cages with Isotropic Cation Reorientation. *Can. J. Chem.* **1990,** *68,* 412–422.

[67] Carabatos-Nedelec, C.; Becker, P. Order-Disorder and Structural Phase Transitions in Solid-State Materials by Raman Scattering Analysis. *J. Raman Spectrosc.* **1997,** *28,* 663–671.

[68] Hagemann, H.; Gomes, S.; Renaudin, G.; Yvon, K., *Raman Studies of Reorientation Motions of $[BH_4]^-$ Anions in Alkali Borohydrides.* J. Alloys Comp. **2004,** 3*63,* 126–129.

[69] Hetmanczyk, J.; Hetmanczyk, L.; Migdal-Mikuli, A.; Mikuli, E. Vibrations and Reorientations of NH3 Molecules in $[Mn(NH_3)_6](ClO_4)_2$ Studied by Infrared Spectroscopy and Theoretical (DFT) Calculations. *Spectrochim. Acta Part A Mol. Biomol. Spectrosc.* **2014,** *136,* 1515–1522.

TOC FIGURE

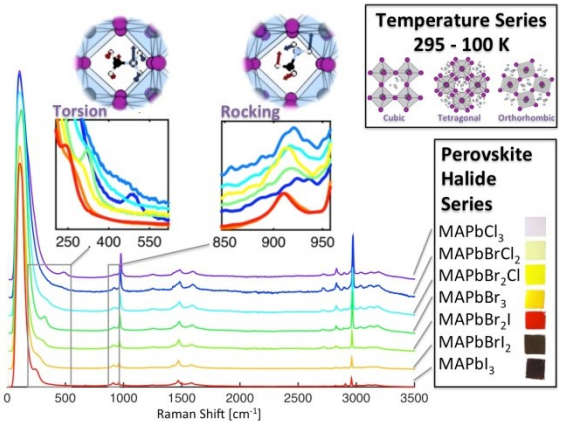
Temperature Series
295 - 100 K
Cubic
Tetragonal
Orthorhombic
Torsion
Rocking
250 400 550
850 900 950
Perovskite Halide Series
MAPbCl3
MAPbBrCl2
MAPbBr2Cl
MAPbBr3
MAPbBr2I
MAPbBrI2
MAPbI3
0 500 1000 1500 2000 2500 3000 3500
Raman Shift [cm-1]